



Effect of ion irradiation on Amorphous and Crystalline Ge-Se and application for phase change temperature sensor IVR

October 2020

Changing the World's Energy Future

Al-Amin Ahmed Simon, Isabella J Van Rooyen, Lyle Jones, Yoshifumi Sakaguchi, Henri Kunold, Maria Mitkova



DISCLAIMER

This information was prepared as an account of work sponsored by an agency of the U.S. Government. Neither the U.S. Government nor any agency thereof, nor any of their employees, makes any warranty, expressed or implied, or assumes any legal liability or responsibility for the accuracy, completeness, or usefulness, of any information, apparatus, product, or process disclosed, or represents that its use would not infringe privately owned rights. References herein to any specific commercial product, process, or service by trade name, trade mark, manufacturer, or otherwise, does not necessarily constitute or imply its endorsement, recommendation, or favoring by the U.S. Government or any agency thereof. The views and opinions of authors expressed herein do not necessarily state or reflect those of the U.S. Government or any agency thereof.

Effect of ion irradiation on Amorphous and Crystalline Ge-Se and application for phase change temperature sensor IVR

Al-Amin Ahmed Simon, Isabella J Van Rooyen, Lyle Jones, Yoshifumi Sakaguchi, Henri Kunold, Maria Mitkova

October 2020

**Idaho National Laboratory
Idaho Falls, Idaho 83415**

<http://www.inl.gov>

**Prepared for the
U.S. Department of Energy
Under DOE Idaho Operations Office
Contract DE-AC07-05ID14517**

Effect of ion irradiation on Amorphous and Crystalline Ge-Se and their application as phase change temperature sensor

Al-Amin Ahmed Simon¹, Lyle Jones¹, Yoshifumi Sakaguchi², Henri Kunold³, Isabella van Rooyen⁴, Maria Mitkova¹

¹Department of Electrical and Computer Engineering, Boise State University, Boise ID 83725, USA

²Neutron Science and Technology Center, Comprehensive Research Organization for Science and Society, Tokai, Naka-gun, Ibaraki, F-319-1106, Japan

³Micron School of Materials Science and Engineering, Boise State University, Boise ID 83725, USA

⁴Fuel Design and Development Department, Idaho National Laboratory, Idaho Falls ID 83415, USA

Keywords: Ion irradiation, Phase change, Temperature sensor, Ion induced damage.

Abstract:

Research on phase change materials is predominantly focused on their application as memory devices or for temperature control which require low phase change temperature. The Ge-Se binary chalcogenide glass system with its wide glass-forming region is a potential candidate for high-temperature and high-radiation phase change applications. This paper reports the concept of employing $\text{Ge}_x\text{Se}_{100-x}$ glasses, to monitor high-temperature (450-528°C) using the phase change effect. Materials selection, device structure and a prototype of sensor performance have been analysed. In addition, the effect of heavy ion irradiation by Xe ions with energy 200, 600, and

1000 keV (Fluence approx. 10^{14} cm^{-2}) over $\text{Ge}_x\text{Se}_{100-x}$ ($x=30, 33, 40$) thin films and phase change devices have been studied. The irradiation effect on the amorphous and crystalline structure of the thin films were evaluated by Raman spectroscopy and XRD. Although the changes in the structural units of amorphous films are negligible, in crystalline films orthorhombic- GeSe_2 crystals are found to be most affected by irradiation and a new phase, orthorhombic- GeSe is found in the thin films after irradiation. The performance of a sensor with an active film of $\text{Ge}_{40}\text{Se}_{60}$ is also shown as an example.

Introduction

The synergy between theoretical/simulation and experimental research has always been very beneficial for a better understanding of materials. So, collaborating and exploring the work of David Drabold, has been a guiding light for (MM) my studies. Notably, preliminary information about what to expect when Ag diffuses in chalcogenide glasses [1–4], the mechanism of diffusion [5,6], how the structure of these glasses is developing [7–9] and the secrets of the phase change effect [10,11]. The phase change effect and the invention of the phase change memory devices based on chalcogenide glasses in 1968 [12] established a new era in the development of the information storage and the study of recrystallization of the disordered systems [13,14]. Although the effects on which the phase change memory devices rely on are well studied, namely crystallization of the disordered active material by a slow increase of its temperature by external stimuli (e.g. heating by Joule effect [15], optical irradiation [16], or external heating sources [17]) they still pose many questions. However, this did not stop the growing research of these materials and newer applications, extending from resistive switching electronic memory [18,19] towards optical memory [20,21]. One of the most applied methods to study phase transition (amorphous to crystalline) is by measuring resistivity, since the

amorphous phase of chalcogenide glass demonstrates dielectric behavior, while the crystalline exhibits excellent conductive characteristics. Usually, there is a well measurable contrast of the resistivity between the phases and is reproducible. The non-isothermal switching to the crystalline phase is typically a speedy process [22], which advances numerous applications based on it. The speed could be attributed to a very short distance, the atoms have to travel for rearrangement [23] because by this solid-solid transition, the system achieves its equilibrium. Moreover, even if the stimuli which transform the system to its crystalline condition are ceased, the material keeps its crystallinity – in this case, its high conductivity state, thus making the effect non-volatile [24,25]. Besides retaining the solid-state, during this phase transition process, the total number of covalent bonds does not change during crystallization. This is an additional reason for the good reliability of devices. The reverse switching goes however through melting the material followed by quenching [26]. Indeed, quenching sounds quite obscure to appear, having in mind that the heating results only in the film, which is located on a substrate at room temperature. However, cooling of the film occurs very fast given that its volume is orders of magnitude smaller than that of the much cooler substrate. Because of this volume difference the heat dissipation from the film appears quite fast and the film vitrifies.

Due to the lack of order, high number of defects and availability of lone-pair electrons on chalcogenide atoms, the electrical properties of chalcogenide glasses are radiation hard. The reason behind this is that the intrinsic defects and the defects caused by irradiation [27] populate in very close proximity and they recombine rapidly. The intrinsic defects manifest themselves as "gap states" in the bandgap of the chalcogenide glasses [28,29]. Near the center of the gap, the states are highly localized so, the electron exchange or hopping probability is low. It was proposed [28,30] that in chalcogenide glasses, these defect states are at dangling bonds D^0 , and the lattice (not in the crystalline but in the network sense) distortion is powerful enough to

produce charged centers D^+ and D^- out of D^0 . Moreover, the lone-pair electrons form the upper portion of the valence band and the D^+ charged centers interact with the neighboring lone-pair electrons. This interaction distorts the environment. The localized states play a vital role in making the chalcogenide glasses radiation hard and indifferent to doping up to some extent. These states behave like recombination centers and traps in the bandgap. A high number of these traps contribute significantly to capture free carriers produced by ionizing radiation. So, it is difficult to move the Fermi level (E_F) either by doping or by irradiation. This is the so-called "Fermi level pinning" phenomenon by which the electrical properties of the material remain stable. This effect is manifested at the performance of many types of devices based on chalcogenide glasses which demonstrate stable operation under irradiation with visible light [31], high-intensity X-rays [32], gamma irradiation [33], as well as irradiation with 50 MeV protons [34] and low-intensity Ar^+ [35].

All the above mentioned incredibly interesting and important properties of chalcogenide glasses and the thermally induced phase change effect in them motivated our study of their function as a temperature sensor in a high-radiation environment to replace traditional sensors like the "Melting Wire". Melt wire sensors are used to measure temperature post factum as they do not supply real-time information. The suggested temperature sensors offer real-time temperature measurements, reversibility and reuse, as well as the option for creation of an array. By combination of several devices built up by different compositions of chalcogenide glasses with different crystallization temperatures, the array could provide data regarding the temperature development.. A similar design has been patented by IBM [36] in 2012. However, its fabrication and application are very much limited by the active material $Ge_2Sb_2Te_5$, which crystallizes at $160^\circ C$. This study is focused on the investigation of the performance of glasses from the Ge-Se system. Although this system is slightly away from the major phase-change memory materials

group studied for electronic switching [37], where low crystallization temperature and fast switching are the key attributes, it has been chosen because of the relatively high crystallization temperature and thermal stability. These make the glasses a good candidate for temperature monitoring of the cladding of Light Water Reactors (LWR) and for metallic or ceramic Sodium Cooled Fast Reactors (SFR) within a temperature range of 400°C to 528°C. In an earlier paper, we presented a detailed study of the crystallization of $\text{Ge}_x\text{Se}_{100-x}$ ($x=30,33,40$) glasses [17] along with a prototype temperature sensor based on optical effects of phase change. In this paper, the focus is on the effect of ion bombardment (emulating neutron irradiation) on the material property and the performance of electrical phase change temperature sensors. The material in the devices changes its solid-state condition (the material crystallizes) after external heating and this effect is measured through the conductivity change by analyzing the current-voltage (I-V) characteristics of the devices. The data about the effect of irradiation with Xe ions over the structure of the active material (Ge-Se glasses) are described and discussed based on three different compositions from the studied system – $\text{Ge}_{30}\text{Se}_{70}$ which is Se-rich member of the Ge-Se glasses, $\text{Ge}_{33}\text{Se}_{67}$ – the stoichiometric composition, and $\text{Ge}_{40}\text{Se}_{60}$ – a Ge-rich material. In the end, the performance of several devices, made with Ge-rich material with reversibility is demonstrated (both as-prepared and irradiated).

Xe ion's choice is based on the fact that xenon is chemically inert, non-radioactive and one of the typical fission products, offering a cost-effective and safer alternative to neutron irradiation. Moreover, since the thermal neutron cross sections of naturally abundant Ge, Se and Al isotopes used in the sensor are quite low (Ge 0.4, Se 0.61 and Al 0.231), the possibility of nuclear transmutation is low and so this study is focused on ion-induced damage only. The other advantages of ion irradiation are: higher damage rate (10^4 times) compared to reactor irradiation

reducing the experimental duration to days instead of decades; the irradiated samples are not radioactive, so post-irradiation characterization cost is reduced; ion irradiation experiments can be controlled better to some extent (e.g., temperature, damage rate, damage level) than reactor irradiation and there's the provision to observe the damage in-situ. However, emulation of neutron irradiation using ion is a new idea and the experiments must be tailored according to the materials and higher control of parameters is needed. This paper could be used as a guideline for material testing by emulating reactor irradiation with well-controlled ion irradiation.

Experimental:

Glass Synthesis

The standard melt quenching technique was used to synthesize bulk chalcogenide glasses. After weighing accurately, the required amount of pure 5N elements were loaded into fused silica ampules. Then the ampules were sealed under vacuum ($\sim 10^{-4}$ mbar) and placed in a programmable tube furnace. To assure the melting of the components, the furnace was programmed depending upon the characteristic temperatures of each composition according to the phase diagram of the Ge-Se system. At the last step, for good glass homogenization, the ampules were kept at 750°C for 144 hours [38]. This temperature is on average 20-50°C above the melting of the synthesized compositions. The importance of the glass melt homogenization arises from the fact that at equilibrium presented in the phase diagrams, glass-forming compositions are usually bordered by congruently melting crystalline phases [39], which can nucleate in melts when quenched and produce microscopic heterogeneities [40]. To ensure the slow aging of the glasses, which is a warranty for the stability of both bulk glasses and thin films, it is important to avoid the formation of microscopic heterogeneities. After 168 hours, the ampules are taken out of the furnace and rapidly cooled in a water-sand bath at room

temperature.

Thin Films and devices Preparation

The chalcogenide glass thin films were prepared by thermal evaporation in a Cressington 308R coating system on thermally oxidized (SiO_2) substrates. The pressure inside the chamber was kept at 10^{-6} mbar and the evaporation rate was $0.3\text{\AA}/\text{s}$. A quartz crystal microbalance was used to estimate the thickness of the films *in situ*. For device fabrication, circular Aluminum electrodes were also deposited by thermal evaporation with the help of a shadow mask on top of the chalcogenide glass film. Figure 1 shows a schematic of a device and its operation [41].

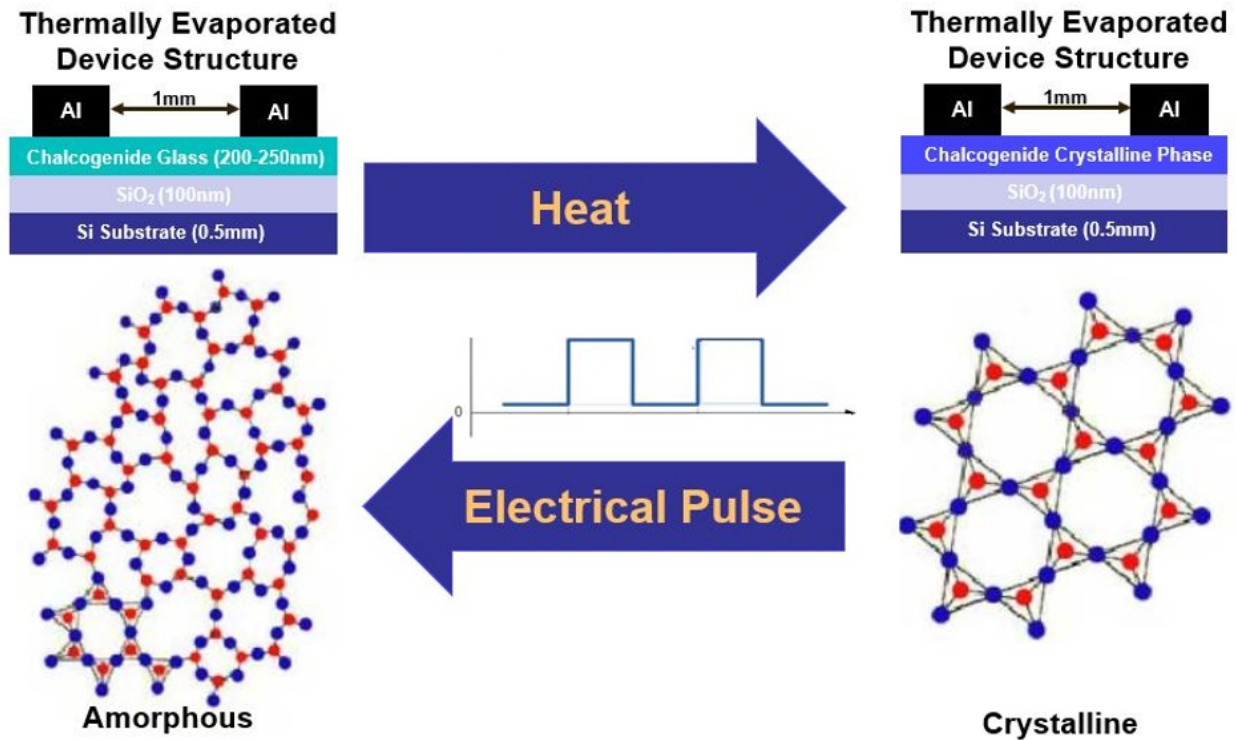


Figure 1: Device Structure and operation [41].

Energy Dispersive Spectroscopy (EDS)

Energy Dispersive Spectroscopy (EDS), used to confirm the exact composition of the produced films, was conducted using a FEI Teneo Scanning Electron Microscope (SEM) with an Oxford Instruments Energy + EDS system. Each sample was measured at five different locations for the collection of an accurate average value and the standard deviation. The study showed that the composition of the thin films deviated ± 1.5 at.% from the composition of the bulk material.

Raman Spectroscopy

To identify any changes in the bonding and physical structure of the materials after irradiation, Raman analysis was performed in a Horiba LabRAM HR Evolution Raman Spectroscopic System in backscattering mode, using a parallel-polarized 632.817 nm He:Ne laser, focused to a spot of 6 μm , with a power of 17 mW. Samples were observed at room temperature and under standard atmospheric pressure.

X-ray Diffraction (XRD) spectroscopy

To investigate the crystalline phases of the thin films, X-ray diffractometer was used. The measurement was done on a Rigaku MiniFlex600 ($\lambda=1.5406\text{\AA}$) at 40 kV and 15 mA. At $10^\circ\text{C}/\text{min}$ scanning rate, the data were collected at room temperature, in a range of $2\theta = 10\text{--}65^\circ$.

Devices Characterization

The devices were characterized in a semiconductor parametric analyzer (Agilent 4155B). I-V characteristics were measured from 0-3 V at a resolution of 30mV/step and the compliance current was set to 50nA. To achieve a phase change of initially amorphous active material, the devices were kept for 15 sec at each temperature, including the onset of crystallization temperature. Crystallized devices were pulsed with a Pulse Generating Unit (PGU) at different

duration for amorphization with square wave amplitude 2V, period 1 μ s, and ON time: 200ns.

Ion Irradiation

Samples from each composition were bombarded with Xe⁺¹/ Xe⁺²/ Xe⁺³ ions, having an initial ion energy 200 keV, 600 keV, and 1000 keV and achieved fluence of 10¹⁴ cm⁻² which corresponds to approximately 5 DPA at each energy level. Ion bombardment was performed with 1.7MV Tandem Particle Accelerator at an angle normal to the surface of each sample using a 100nA beam current and chamber pressure of 10⁻⁸ Torr.

Displacement per atom (DPA) calculation

With the help of - The Stopping and Range of Ions in Matter (SRIM) simulation software, the calculation of the DPA was done. SRIM is a group of programs that calculate the stopping and range of ions (up to 2 GeV/amu) into the matter. The software uses a quantum mechanical treatment of ion-atom collisions (assuming a moving atom as an "ion", and all target atoms as "atoms"). To make the calculation efficient, statistical algorithms that allow the ion to make jumps between calculated collisions and then averaging the collision results over the intervening gap are used. Among the programs, the Transport of Ions in Matter (TRIM) accepts complex targets made of compound materials with up to eight layers. It calculates the final 3D distribution of the ions as well as kinetic phenomena associated with the ion's energy loss like target damage, sputtering, ionization, and phonon production [42].

For simplicity of the simulation, TRIM has the option to utilize "Kinchin-Pease Approximation" to calculate ion-induced damage. In this paper, this approximation was used where no spatial extension of the damage after the first recoil is initiated since full cascade was not calculated. So, all the damage is calculated, assuming it only occurs during the initial collision [43]. Moreover, ions were incident on the thin films and devices at a normal angle and since the fluence (10¹⁴

cm⁻²) is much lower than the atomic density (10^{22}cm^{-3}) of Ge-Se, the sputtering was neglected. At room temperature, most of the implantation damage normally "self-anneals", because the atoms have enough energy to allow simple target damage to regrow into its original form at room temperature. However, since there are no thermal effects in TRIM, the damage which is calculated is the one that would happen for implantation at 0 K. Although, ignoring the thermal effects changes the quantity of final damage, the basic damage types still occur.

Ion irradiation introduces displacements of atom in a material. Both vacancies (empty lattice site which was originally occupied) and replacement collisions (atom sites with a new atom identical to the original atom) are considered as displacement. From full cascade simulation, it is seen that for all the irradiation conditions, replacement collision is one order of magnitude lower than total vacancies produced and so it was not considered.

An example of DPA calculation is shown below and all calculations are presented in Table 2.

Damage rate, Time, Fluence and DPA calculation:

(For maximum damage rate from SRIM simulation for Ge₄₀Se₆₀, from Figure. 8)

Atomic Density, [Calculated from SRIM, considering density 4.38gcm^{-3} , from Figure. 7]

Current = $1\mu\text{A}$ [From experimental setup]

Charge of the ion, $q = +1$ for $+1$ ions, and $e =$

$Q = q \cdot e$

Area, (From experimental setup)

So, to induce (for example) 5 DPA of damage on 250 nm Ge₄₀Se₆₀ on SiO₂ with 200keV Xe¹⁺ ions, where the sample area, A is going to take

sec

=3108 sec

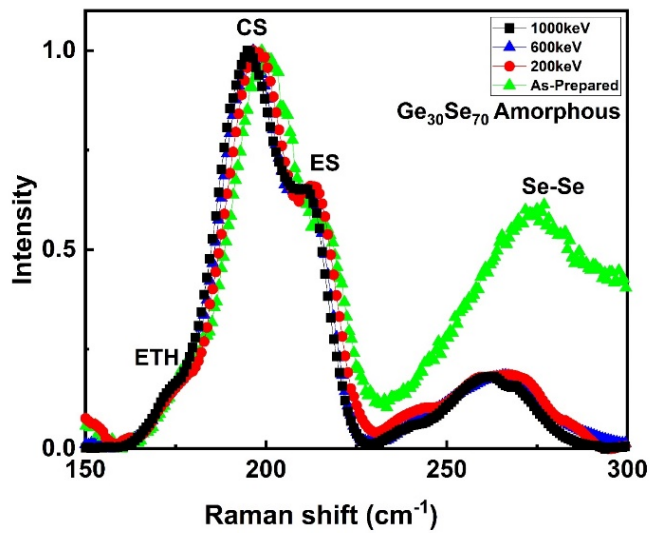
=52 min

=

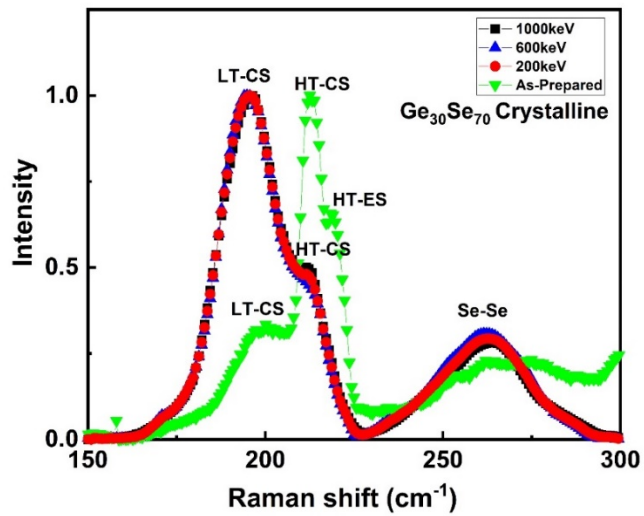
Results:

As mentioned before, it is expected that during irradiation, microstructural deformation and defects will be recombined up to some extent. Raman spectroscopy of the amorphous thin films confirms this hypothesis. It is seen that the $\text{Ge}_{30}\text{Se}_{70}$ glass Figure 2(a) is built predominantly by Corner Sharing (CS) and Edge Sharing (ES) tetrahedra and Se chains (CH). The presence of such structural units is proved by the high-frequency bands A_I and A_I^C at 200 cm^{-1} (CS) and 219 cm^{-1} (ES), respectively. The occurrence of Se chains is demonstrated by the vibration spectra at $230\text{-}280\text{ cm}^{-1}$ [44,45]. After irradiation with 200 keV, the Raman spectra demonstrate an increased areal intensity of the Se-Se chain mode and breaking of the ES building blocks, which at higher irradiation are restored and at irradiation with 1000 keV their aerial intensity related to the areal intensity of the CS units is close to the initial one before irradiation although their absolute values are smaller - Figure 2(a). The crystalline structure- Figure 2(b), firmly demonstrates phase change and crystalline structure characteristic for the low temperature (LT) polymorph form of GeSe_2 [46]. However, this crystal structure loses stability after irradiation, the Raman modes undergo low energy shift, which is characteristic of the modes arising from a more disordered structure. With the increase of the irradiation energy, the formation of ES breathing mode becomes more prominent, which is an indication for

crystallization of the high temperature (LT) polymorph form of GeSe.



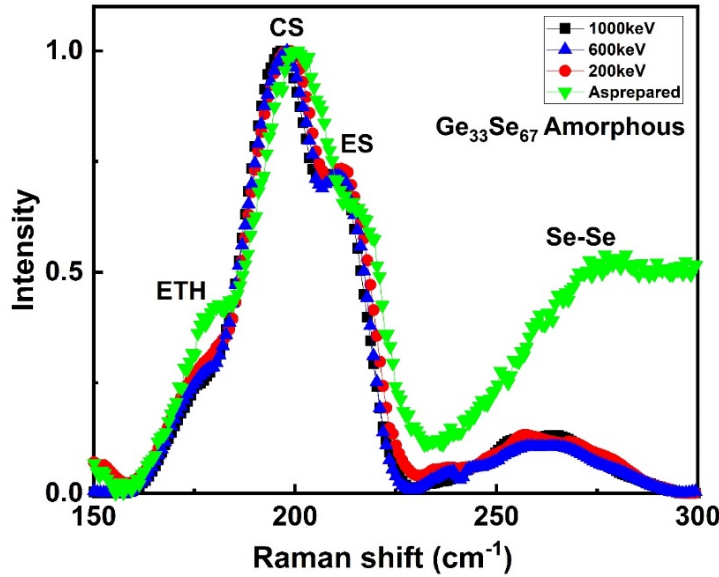
a)



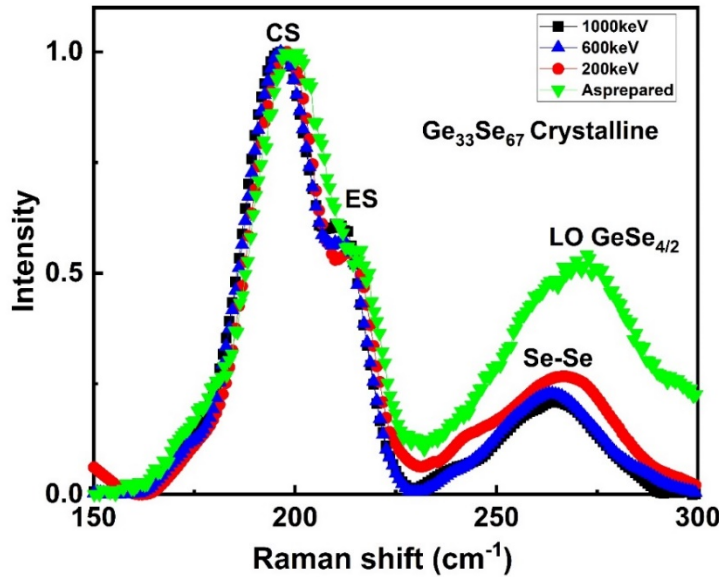
b)

Figure 2: Raman spectra of $\text{Ge}_{30}\text{Se}_{70}$ under different irradiation. a) Amorphous b) Crystalline.

In addition to CS, ES and Se-Se peak, $\text{Ge}_{33}\text{Se}_{67}$ thin films exhibit a distinct peak in Figure 3(a) around 178cm^{-1} , which indicates vibrations of Ge-Ge bonds representing the formation of ethane-like structure $\text{Ge}_2(\text{Se}_{1/2})_6$ (ETH) [47]. After irradiation, a reduction of both Ge-Ge and Se-Se aerial peak intensity is seen along with an increase in ES peak intensity, suggesting structural reorganization and consuming the wrong bonds for the formation of ES structures. The Raman spectra of as-prepared crystallized films in Figure 3(b) exhibit only well-expressed CS vibrations, characteristic for the HT GeSe_2 polymorph form. After irradiation, structural transformation occurs by which formation of ES vibrations are well shaped on the Raman spectra, indicating crystallization of LT GeSe . This effect is accompanied by a decrease in the areal intensity of the Se-Se chain mode.



a)

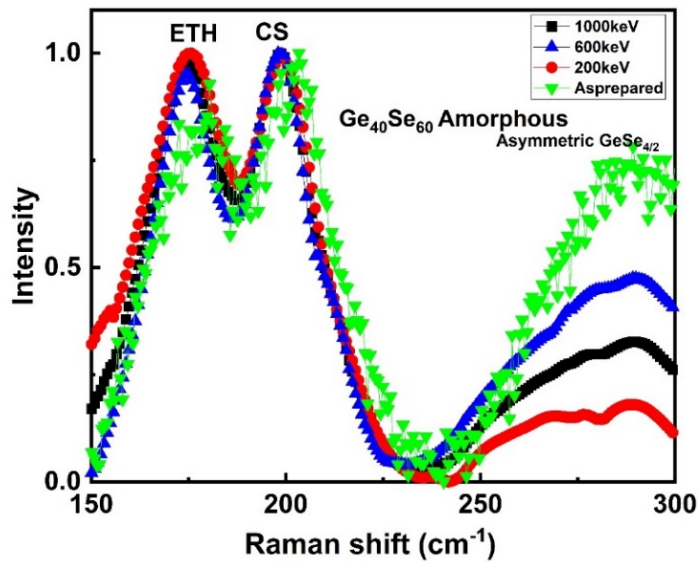


b)

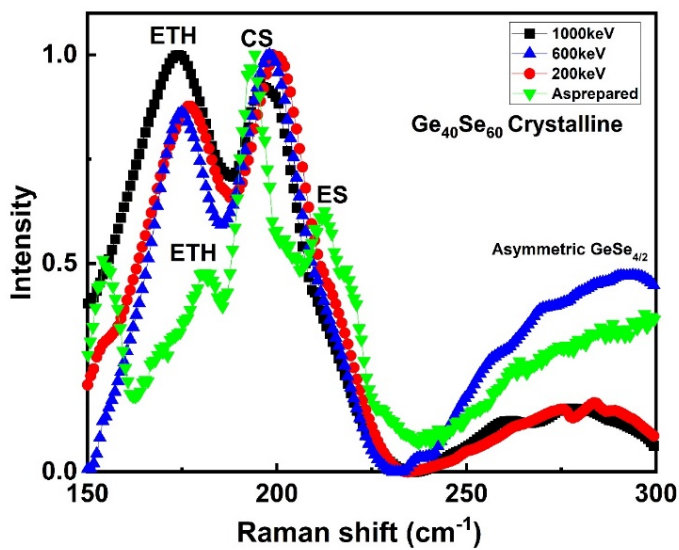
Figure 3: Raman spectra of $\text{Ge}_{33}\text{Se}_{67}$ under different irradiation. a) Amorphous b) Crystalline.

As expected, the ETH structure dominates in the Raman spectra of the $\text{Ge}_{40}\text{Se}_{60}$ films in Figure 4(a). Moreover, the vibrational band in the range of 270 cm^{-1} to 310 cm^{-1} can be fitted with one Gaussian, which implies the presence of only one type of structural unit. The size of the vibrational mode and the composition suggest that it is unrealistic to consider this vibrational band is occurring from Se-Se chains which are energetically not favorable [48]. It is more logical to consider this vibration as rather related to asymmetric vibrations of tetrahedral structures containing Ge and Se. So, we suggest that these vibrations are related to asymmetric ES breathing mode. Based on this hypothesis, the Ge-rich glasses are anticipated to be quite phase-separated. Up to 1000 keV energy, these films keep their basic structure. However, at irradiation with 1000 keV, the structure is totally destroyed, representing only CS and ES vibrations simultaneously with a substantial decrease of the areal intensity around 267 cm^{-1} . The

non-irradiated crystals suggest the formation of the LT GeSe_2 in Figure 4(b). After irradiation, there is a growth of the areal intensity at lower energy, which suggests a strong development of CS and ES structural units, leading to the formation of the LT GeSe .



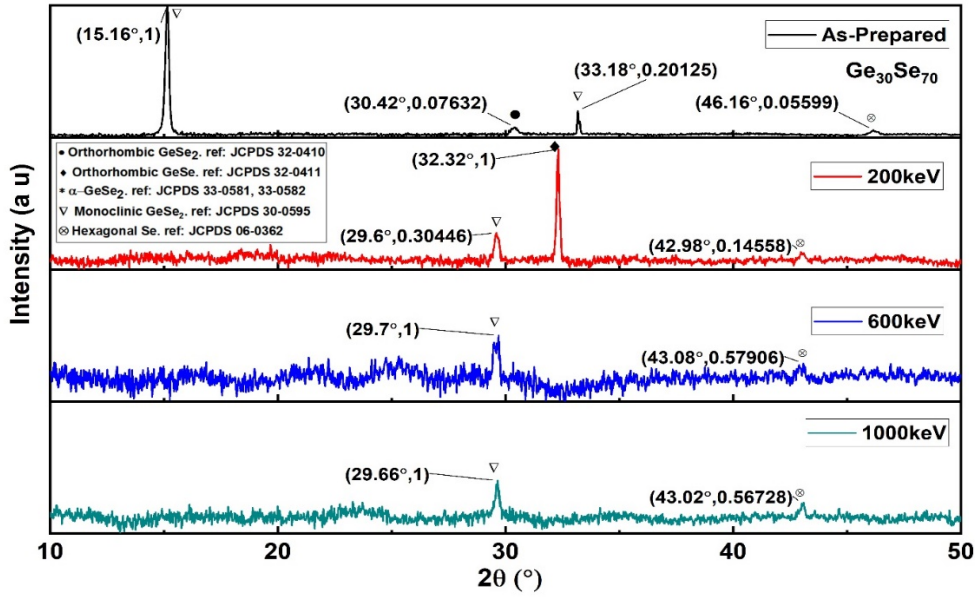
a)



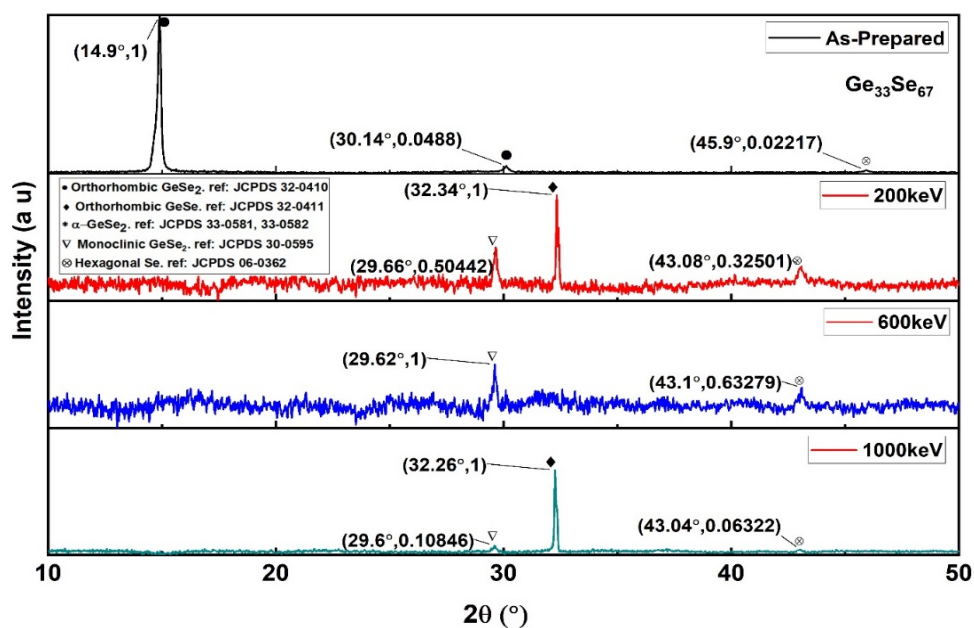
b)

Figure 4: Raman spectra of $\text{Ge}_{40}\text{Se}_{60}$ under different irradiation. a) Amorphous b) Crystalline.

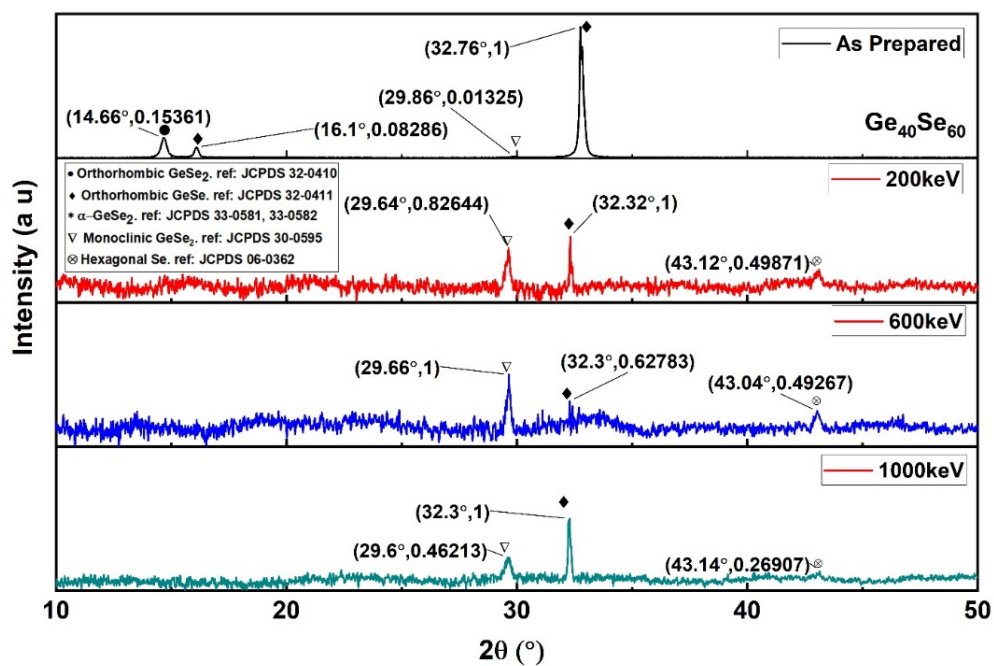
The XRD spectra of the crystallized thin films are presented in Figure 5(a-c).



a)



b)



c)

Figure 5: XRD of irradiated and as-prepared crystallized thin films. a) $\text{Ge}_{30}\text{Se}_{70}$ b) $\text{Ge}_{33}\text{Se}_{67}$ c) $\text{Ge}_{40}\text{Se}_{60}$

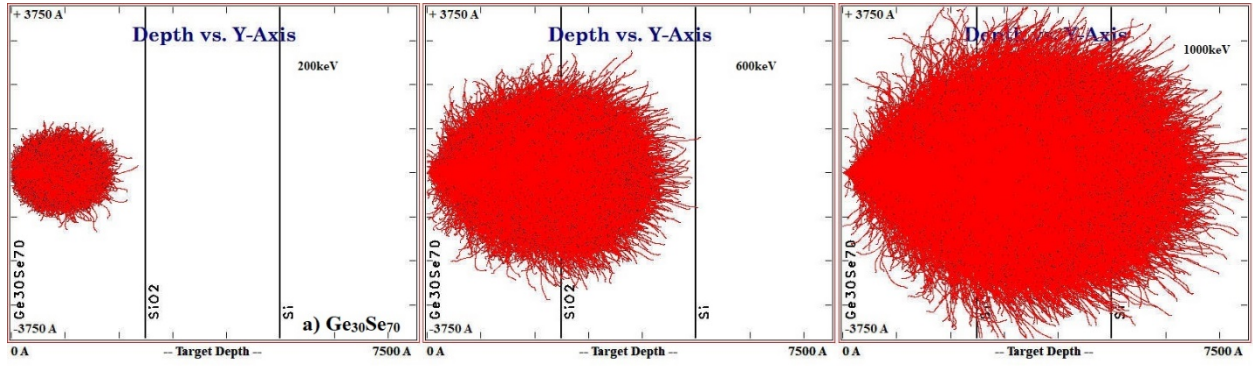
The XRD data confirm the Raman results in this that they demonstrate a presence of the LT GeSe_2 phase at the initial crystallization, which then is transformed into an LT GeSe phase. Hexagonal Se is present in all thin films and its crystal size is related to the availability to form wrong bonds after irradiation. In many cases, GeSe crystals are also present and although their appearance seems to be very sporadic, it needs in-depth discussion. In $\text{Ge}_{30}\text{Se}_{70}$, GeSe is not present in the as-prepared film. It only emerges after 200 keV irradiation and after 600 and 1000 keV, the GeSe peak is missing - Figure 5(a). In $\text{Ge}_{33}\text{Se}_{67}$, the GeSe peak emerges after 200 keV irradiation and is missing only for 600keV – Figure 5(b). In $\text{Ge}_{40}\text{Se}_{60}$, all three peaks are present for each condition – Figure 5(c). But for 600keV, the GeSe peak suggests the formation of crystals with the smallest size. To further understand the effect of irradiation, the size of the crystals was calculated (Table 1).

Discussion:

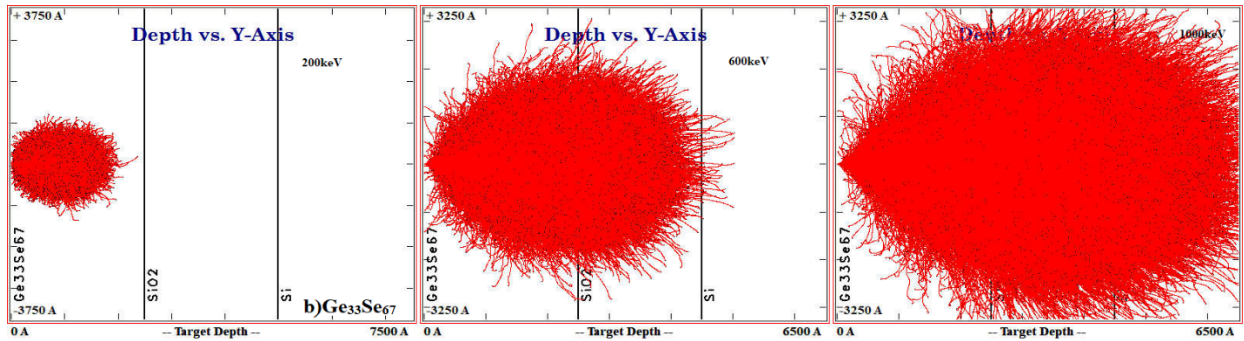
Traveling through solids ions interact/collide with stationary atoms and change their initial trajectory. While traveling, they also lose energy in radiative processes. Since the radiative processes like bremsstrahlung and Cherenkov radiation are very limited for ions, they can be neglected. In addition, ions can pick up electrons from various shells and become a very slow-moving ion going through cascade collisions and ultimately stop. So, there are two types of energy transfer mechanisms involved i) elastic scattering: collision of nuclei, and ii) inelastic collision: excitation and ionization of atoms. Typically, when ion energy is below 10keV/amu,

elastic scattering dominates [49].

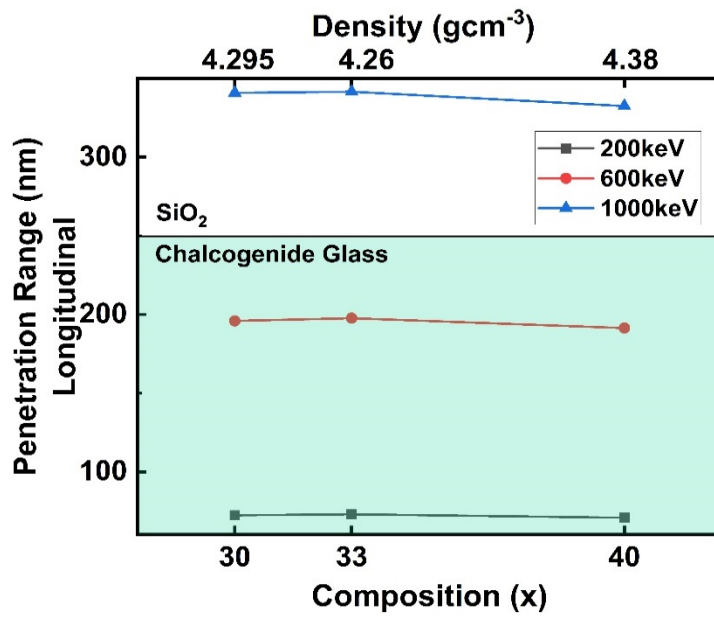
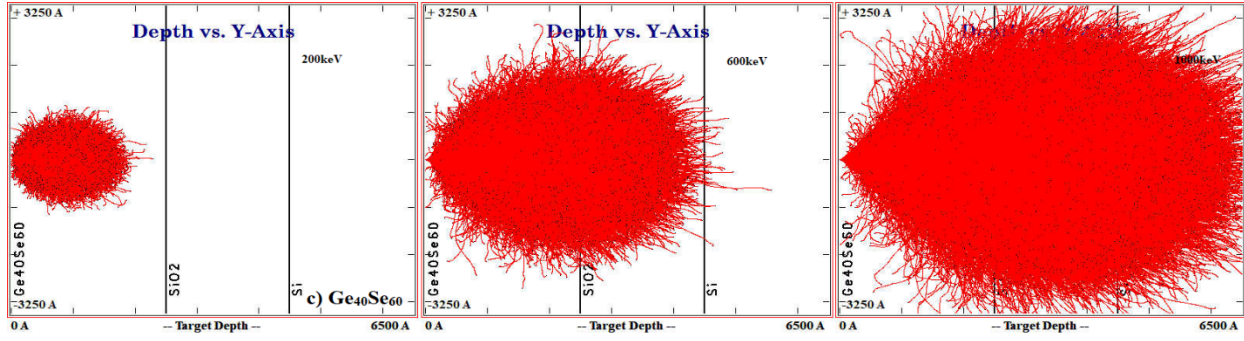
TRIM simulation showed the penetration range of the Xe ions in different compositions. The TRIM simulation of the Xe ions interaction example of which is shown in Figure 6 for $\text{Ge}_{40}\text{Se}_{60}$ demonstrates that at the chosen fluence, ions with energy 200 keV (1.53 keV/amu) penetrate only in the chalcogenide glass film, the ions with energy 600 keV (4.58 keV/amu) reach the SiO_2 film and stop close to the interface ChG/ SiO_2 and those with 1000 keV (7.65 keV/amu) energy penetrate the SiO_2 substrate. It should be noted here that - Figure 6 shows both the range of the ions (d) and actual depths (a-c).



a) $\text{Ge}_{30}\text{Se}_{70}$



b) $\text{Ge}_{33}\text{Se}_{67}$



c) $\text{Ge}_{40}\text{Se}_{60}$

d)

Figure 6: Ion penetration depth in chalcogenide glass (a-c) actual from simulation, (d) range.

This is characteristic for all studied compositions with small variations in the particular penetration depth, which depends upon the density of the chalcogenide glass (Figure 7 [50]) which is one other factor to be considered.

The simulation shows that the longitudinal penetration range increases with ion energy and decreases with the density of the material. The peak damage rate calculated from TRIM shows an opposite to the penetration pattern in Figure 8. Damage goes lower with energy and is proportional to the density. We suggest that with more energy, the ions penetrate further and more interaction happens at the interface or in the substrate. Also, ions interact more with denser materials, since they come in contact with a higher number of atoms, hence higher damage rate in $\text{Ge}_{40}\text{Se}_{60}$.

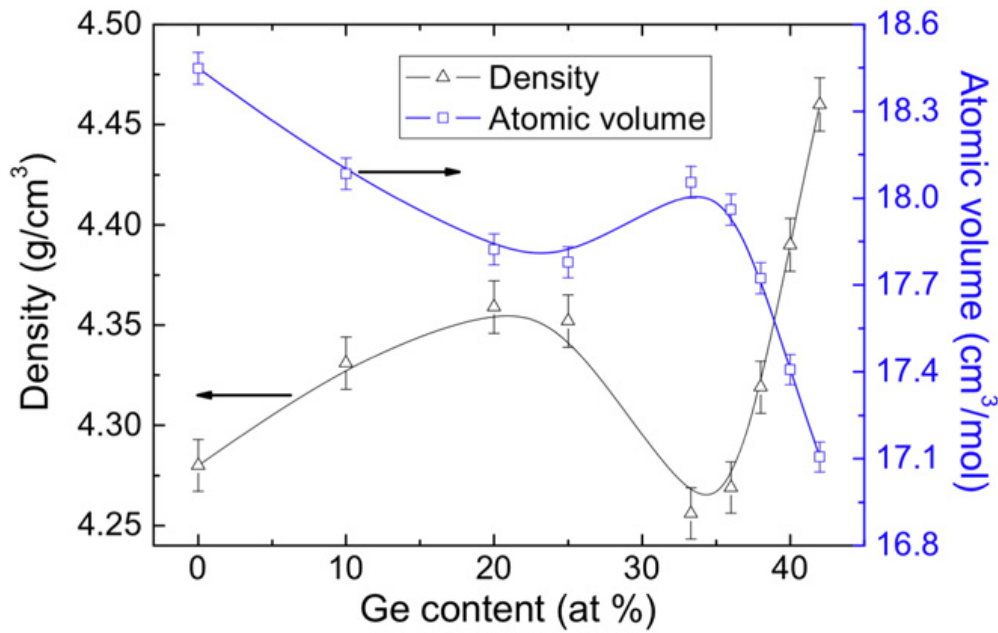


Figure 7: Composition vs density and volume [50].

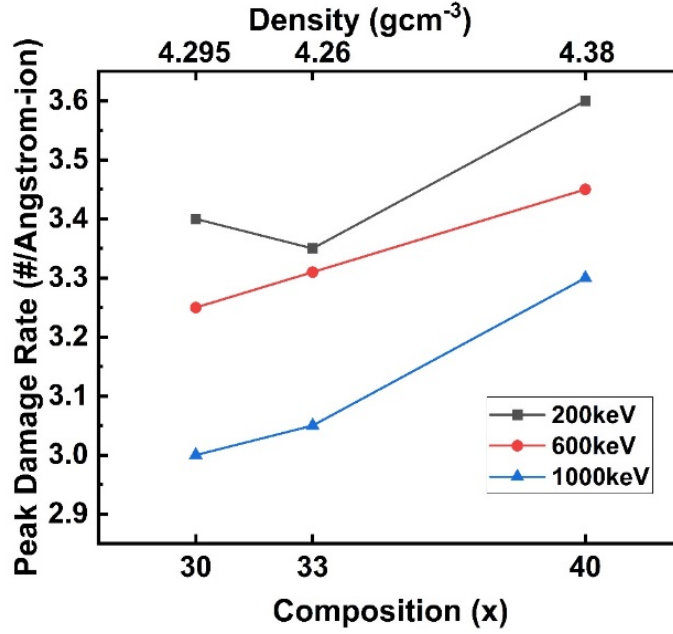


Figure 8: Peak damage rate vs composition.

Another important factor here is the size of the atoms compared to the ions. The Xe^+ ion (1.08 Å) is smaller than Ge atoms (1.25 Å) but similar to Se atoms (1.03 Å) [51]. The effect is clear from the simulation— Figure 9, which shows only for Ge-rich glass $\text{Ge}_{40}\text{Se}_{60}$, Ge target vacancy was higher than for Se. This phenomenon plays an important role in irradiated crystalline films.

Due to the amorphous nature of the glassy films, the effect of irradiation is not so prominent. But the crystalline films showed the effect of the irradiation clearly. Since Se can be displaced more than Ge, due to the ion/atom size equality, it was expected that the Se-rich composition $\text{Ge}_{30}\text{Se}_{70}$, will be most affected by the irradiation. For this composition, two important factors interplay during the interaction with ions. On one hand, the structural stability of the Se-rich $\text{Ge}_{30}\text{Se}_{70}$ amorphous films – Figure 2(a,b). This is mainly based on their floppiness

[52], which allows an easy arrangement of the structural units during external stimuli by changing the angles under which the tetrahedra are organized without affecting the basic ratio of the structural units. On the other hand, the cation-cation distance, in this case, is smaller than in the stoichiometric composition as revealed by XPS studies [53] and so the interaction with the Xe ions will be much stronger compared to with smaller ions, like Kr ions for example [54]. Figure 5(a) shows that a very dominant peak of orthorhombic GeSe is present after irradiation with 200 keV ions. This is an indication of the formation of Se deficient structure. However, the GeSe peak is missing at irradiation with 600 and 1000 keV. In addition to having the smallest size of GeSe crystals compared to the other two compositions, this could also mean that the GeSe crystals form near the glass-substrate interface, and since higher energy ions penetrate further, these crystals are affected. The Raman spectra at these conditions exhibit well expressed ES structure formation. This indicates the presence of crystals with structure combining CS and ES building blocks, which is characteristic of the LT polymorph form of GeSe [46,55]. It indeed has been registered on the XRD spectra – Figure 5(a) with growing crystal size as a function of the irradiation energy.

Regarding the $\text{Ge}_{33}\text{Se}_{67}$ composition, the interaction with the Xe ion affects mainly the Ge-Ge bonds (bond enthalpy 263.6 kJ/mol) [56] in the ETH like structure and facilitates the reaction of the newly formed Ge dangling bonds with Se atoms from the Se chains. The irradiation with higher energy leads to phase separation and redshift of the tetrahedral breathing modes, giving rise to the appearance of the A_1 breathing mode at 200 cm^{-1} , characteristic for the LT phase of GeSe_2 , [55] and well expressed Se-chain mode. It is important to note that in the crystalline phase, the A_1^C mode appearing at 218 cm^{-1} . Figure 3(a) indicates the presence of ES tetrahedra and this structure is preserved during the irradiation. The predominant formation of heterobonding in the network explains the structural stability of this composition after irradiation, as

presented in the Raman data – Figure 3(b). Indeed due to the Ge/Se ratio, which in the ideal case would lead to the formation of a particular number of only CS and ES tetrahedra, the structure of both – the amorphous and crystalline phases remains very stable during the irradiation with Xe ions after the Ge-Ge bonds collapse. This new structure occurring after irradiation brings about to formation after crystallization of LT Gese - Figure 5(b). We suggest that the formation is due to the interaction of the Ge-Se network with the Xe ions. Xe replaces some of the Se atoms and depletes the Ge-Se matrix of selenium as discussed for Se rich composition. A similar effect has been registered in [57] with increasing Ge concentration in the films. Here one more phenomenon needs explanation – the lack of formation of GeSe at irradiation with 600 keV. We suggest this is due to the reasons already explained about the $\text{Ge}_{30}\text{Se}_{70}$ composition but in this case there is a clear appearance of GeSe crystals at 1,000keV irradiation. The stoichiometric composition $\text{Ge}_{33}\text{Se}_{67}$ is the least dense among all the studied glasses - Figure 7. Nevertheless, its density is still higher than that of SiO_2 (2.27g/cm^3) and Si (2.33 g/cm^3) [58,59]. So, there would be massive penetration of Xe ions which reach the Si substrate where repulsion of charged species can occur. It is for this reason that the Raman spectrum at the highest irradiation energy shows biggest damage of the amorphous structure – Figure 3(b) and consequently forms Se-depleted GeSe crystals - Figure 5(b).

The amorphous Ge rich composition $\text{Ge}_{40}\text{Se}_{60}$ displays big structural stability, although there are expectation was that the interaction with the Xe ions will be the strongest due to its closest packaging and highest density [55]. However, Wang et al. [60] gave evidence that the Ge rich structure is quite phase separated. As revealed by TRIM simulation – Figure 9, in the area of Ge-Ge bonding, the interaction with the incoming ions would be limited because of the bigger size of Ge atoms and hence the lower density seen by the Xe ions. The networks beyond the chalcogenide film (the SiO_2 film and the Si substrate), which are reached by the ions with the

energy of 600 keV and 1000 keV respectively, provide channels for these ions because of their lower density. Hence, Xe ions interact only with the higher density clusters in the chalcogenide glass matrix and escape to the lower density regions (SiO_2 and Si) affecting the chalcogenide network only at the highest energy used. Similarly, in the crystalline phase unstable crystalline organization before irradiation is seen. But after irradiation the structural organization is left unbroken even at highest irradiation energy giving rise to LT Gese crystalline in accordance with the results reported by Wang et al. [45]. Figure 9 shows that for this composition, the number of the Ge vacancies is much higher than the number of Se-vacancies which is an exception compared to the other compositions. Although from the chemical point of view, we consider $\text{Ge}_{40}\text{Se}_{60}$ as Ge-rich, from the atomistic point of view there are more Se than Ge atoms in all regarded compositions. Moreover, Se is heavier than Ge and it would have been more intuitive if Ge showed more vacancies at even $\text{Ge}_{33}\text{Se}_{67}$. We propose that for $x \leq 33$, the damage/vacancy is "size-dependent" and for $x \geq 33$, the damage is "mass-dependent". From - Figure 9, it is also evident that with higher density, we get higher damage. So, the whole ion-matter interaction is a multivariate multiphysics problem that becomes much more complex when it comes to irradiating crystalline materials. In addition to all of these phenomena, surprisingly the crystalline materials have been known to change to a different crystal phase after irradiation [61], [62,63] and such transition is observed in our case. Experiments suggest that ion irradiation is also a stabilizing process for such a phase transition [64]. In this case, the main reason for this stability is that the ES structure requires less energy to form and their formation opens the structure [65] which reduces the opportunity for crystal damage by the incoming Xe ions.

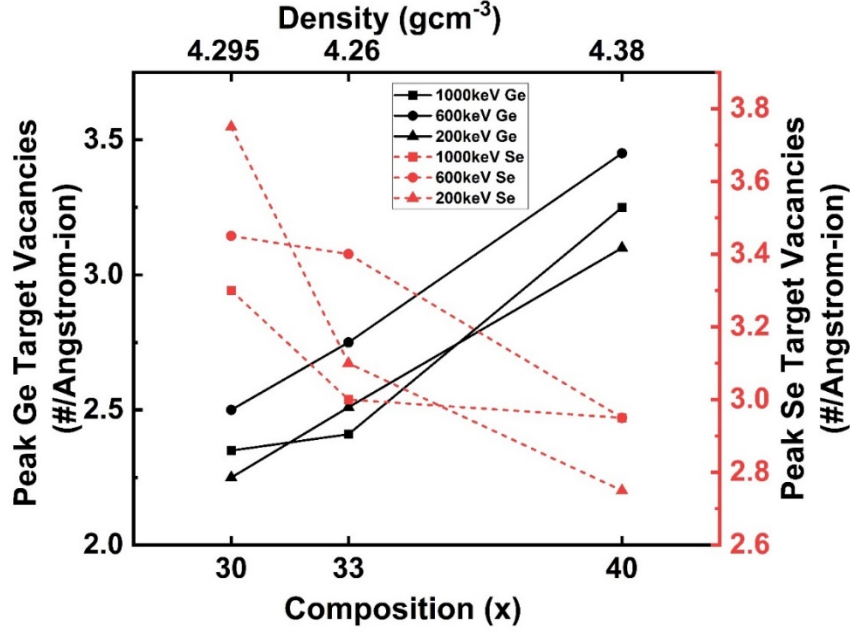
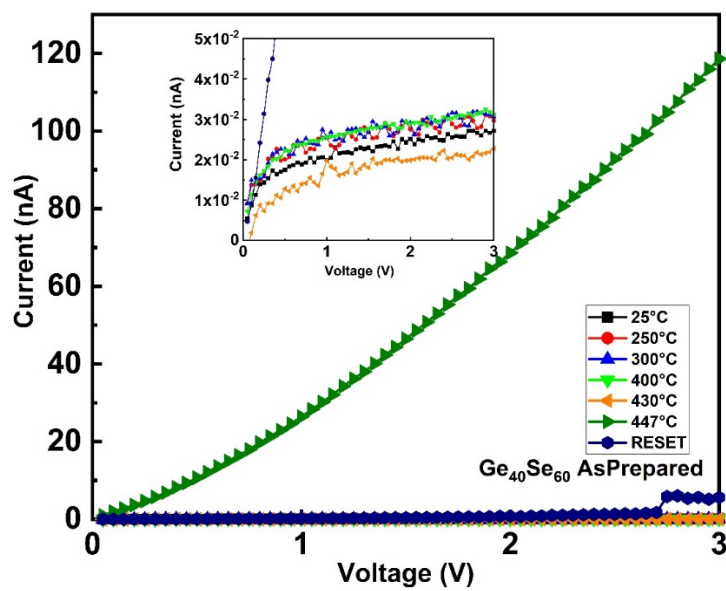
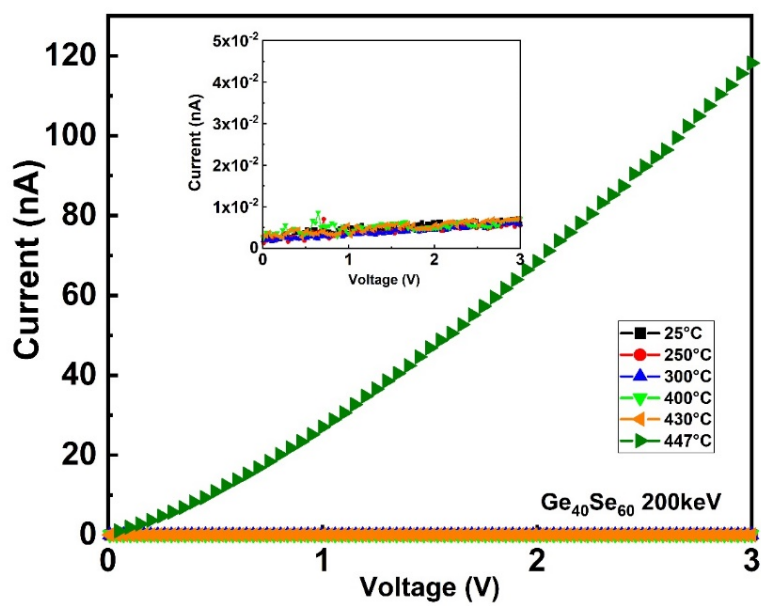


Figure 9: Vacancy produced in Germanium and Selenium atoms.

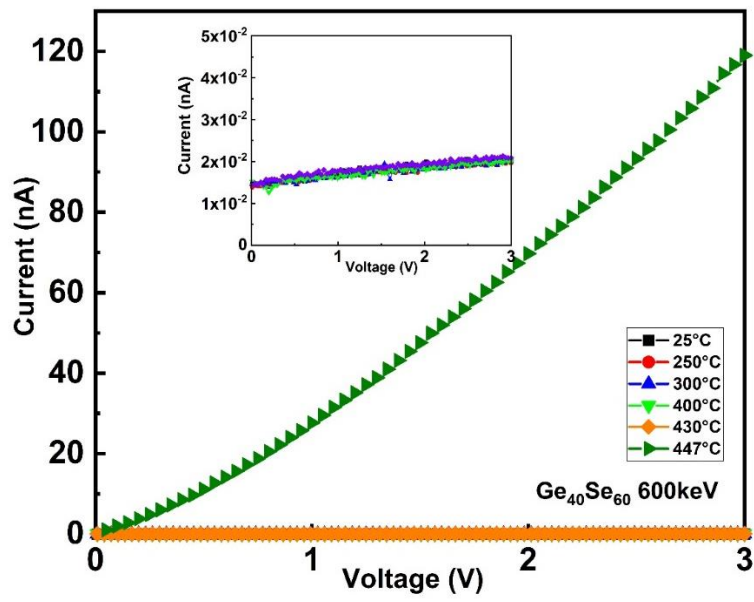
A proof of concept for application of phase change effect for temperature monitoring under irradiation with Xe ions was given by testing a batch of prototypes of a phase change temperature sensor - Figure 10. Those are devices based on $\text{Ge}_{40}\text{Se}_{60}$ composition. The current-voltage characteristics of devices are stable without any significant changes in the current up to the onset of crystallization. After 15 sec of heating at the onset of crystallization temperature, the current of the devices rises significantly (ON state) compared to the one for the amorphous (OFF state) phase ($I_{\text{on}}/I_{\text{off}} = 10^3$) and from the I-V characteristic it is evident that the conduction mechanism has also changed, as in the ON state shows Ohmic characteristic. The as-prepared devices were reversed (RESET) by electrically pulsing them for 10min. A closer look at the I-V characteristic shows that the reversed devices' conductivity is within the frames of the initial device performance (inset of Fig. 10). Further research is required to optimize and establish the parameters of reversibility.



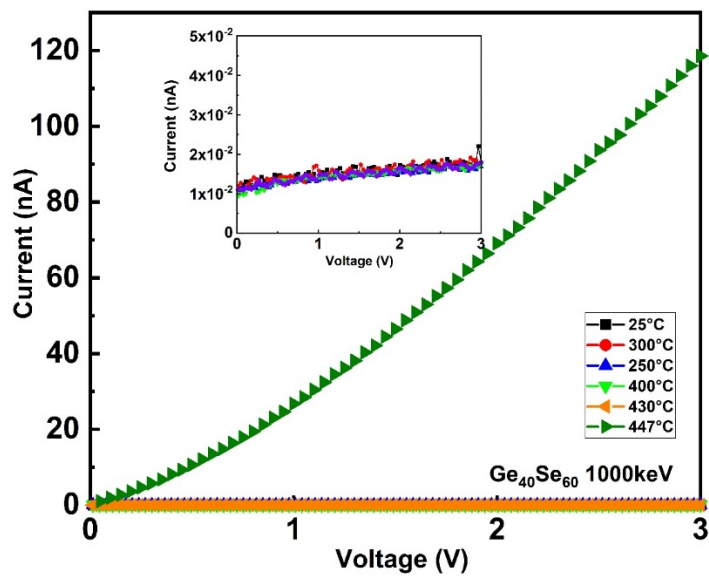
a)



b)



c)



d)

Figure 10: Ge₄₀Se₆₀ Device Characterization. a) As prepared b) 200keV c) 600keV d)1000keV

This process should be much easier for the irradiated cases having in mind the amorphization of the crystalline phases occurring during the ion–chalcogenide films interaction. The OFF state conductivity of the irradiated devices is very stable. This is not a surprise considering the structural stability of this composition demonstrated in the Raman spectra obtained at different irradiation doses. Because of the structural inhomogeneity of this composition and the expected fluctuation of the interactions with the Xe ions, the average of the OFF state current is not a function of the irradiation energy which is within 10^{-2} nA and keeping the ON/OFF current ratio stable.

Conclusion

The collected data presented here draw a complete picture of the application of Ge-Se chalcogenide glasses in a high-radiation environment as a temperature sensing material. From TRIM simulation, ion irradiation parameters are chosen to study the effect of chalcogenide glass, glass/insulator interface and Si substrate. This study reveals that irradiation with Xe ions, although introducing some small changes in the structure of the studied amorphous phases, they remain stable even at high irradiation energies. More expressed structural changes occur in the crystalline phases which in the course of irradiation change their structure from LT GeSe₂ to LT GeSe. This stabilizes it and opens up the structure reducing the damaging effects in it. From XRD data, the evidence of ion-irradiation induced crystal-crystal phase change in crystalline Ge-Se thin films is found. The emergence of Se-depleted, orthorhombic-GeSe transition has been attributed to complex interaction of Xe ion size, energy, density and temperature. From the presented devices, it is seen that the OFF currents are within 10^{-2} nA with or without irradiation

and the ON/OFF current ratio is 10^3 which is considerably high.

Acknowledgment

This work was financially supported by the US Department of Energy (DOE), grant number DOE-NE 0008691 and DOE-NSUF grant, 19-2832. The authors gratefully acknowledge DOE's contribution to the advancement of their research. The authors also acknowledge the usage of the Raman spectroscopy system at Boise State Surface Science Lab.

References

- [1] B. Prasai, M. E. Kordesch, D. A. Drabold, and G. Chen, *Physica Status Solidi (b)* 250, 1785 (2013).
- [2] K. Prasai and D. A. Drabold, *Nanoscale Research Letters* 9, 594 (2014).
- [3] K. Prasai, G. Chen, and D. A. Drabold, *Phys. Rev. Materials* 1, 015603 (2017).
- [4] D. Igram, H. E. Castillo, and D. A. Drabold, *Journal of Non-Crystalline Solids* 514, 1 (2019).
- [5] D. N. Tafen, D. A. Drabold, and M. Mitkova, *Physica Status Solidi (b)* 242, R55 (2005).
- [6] D. N. Tafen, D. A. Drabold, and M. Mitkova, *Phys. Rev. B* 72, 054206 (2005).
- [7] F. Inam, D. N. Tafen, G. Chen, and D. A. Drabold, *Physica Status Solidi (b)* 246, 1849 (2009).
- [8] G. Chen, F. Inam, and D. A. Drabold, *Appl. Phys. Lett.* 97, 131901 (2010).
- [9] B. Cai, X. Zhang, and D. A. Drabold, *Phys. Rev. B* 83, 092202 (2011).
- [10] B. Cai, B. Prasai, and D. A. Drabold, *Flash Memories* (2011).
- [11] B. Prasai and D. A. Drabold, in *Molecular Dynamics Simulations of Disordered Materials: From Network Glasses to Phase-Change Memory Alloys*, edited by C. Massobrio, J. Du, M. Bernasconi, and P. S. Salmon (Springer International Publishing, Cham, 2015), pp. 511–524.
- [12] S. R. Ovshinsky, *Phys. Rev. Lett.* 21, 1450 (1968).
- [13] F. H. Stillinger and P. G. Debenedetti, *Annual Review of Condensed Matter Physics* 4, 263 (2013).
- [14] T. Yanagishima, J. Russo, and H. Tanaka, *Nature Communications* 8, 15954 (2017).
- [15] G. W. Burr, M. J. Brightsky, A. Sebastian, H.-Y. Cheng, J.-Y. Wu, S. Kim, N. E. Sosa, N. Papandreou, H.-L. Lung, H. Pozidis, E. Eleftheriou, and C. H. Lam, *IEEE Journal on Emerging and Selected Topics in Circuits and Systems* 6, 146 (2016).
- [16] A. R. Barik, M. Bapna, D. A. Drabold, and K. V. Adarsh, *Sci. Rep.* 4, 1 (2014).
- [17] A.-A. Ahmed Simon, B. Badamchi, H. Subbaraman, Y. Sakaguchi, and M. Mitkova, *J Mater Sci: Mater Electron* 31, 11211 (2020).

- [18] W. Welnic, A. Pamungkas, R. Detemple, C. Steimer, S. Blügel, and M. Wuttig, *Nature Materials* 5, 56 (2006).
- [19] Y. Imanishi, H. Hayashi, and T. Nakaoka, *J Mater Sci* 53, 12254 (2018).
- [20] M. Wuttig and N. Yamada, *Nature Materials* 6, 824 (2007).
- [21] A. V. Kolobov, P. Fons, A. I. Frenkel, A. L. Ankudinov, J. Tominaga, and T. Uruga, *Nature Materials* 3, 703 (2004).
- [22] A. V. Kolobov, P. Fons, and J. Tominaga, *Scientific Reports* 5, 13698 (2015).
- [23] P. Guo, A. M. Sarangan, and I. Agha, *Applied Sciences* 9, 530 (2019).
- [24] D. Adler, M. S. Shur, M. Silver, and S. R. Ovshinsky, *Journal of Applied Physics* 51, 3289 (1980).
- [25] P. Noé, A. Verdy, F. d’Acapito, J.-B. Dory, M. Bernard, G. Navarro, J.-B. Jager, J. Gaudin, and J.-Y. Raty, *Science Advances* 6, eaay2830 (2020).
- [26] J. Takeda, W. Oba, Y. Minami, T. Saiki, and I. Katayama, *Appl. Phys. Lett.* 104, 261903 (2014).
- [27] T. Kavetsky, O. Shpotyuk, V. Balitska, G. Dovbeshko, I. Blonsky, I. Kaban, W. Hoyer, M. Iovu, and A. Andriesh, in *Sixth International Conference on Advanced Optical Materials and Devices (AOMD-6)* (International Society for Optics and Photonics, 2008), p. 71420B.
- [28] R. A. Street and N. F. Mott, *Phys. Rev. Lett.* 35, 1293 (1975).
- [29] S. R. Ovshinsky, E. J. Evans, D. L. Nelson, and H. Fritzsche, *J OVONIC RES* 15, 311 (1968).
- [30] T. Shimizu, *Jpn. J. Appl. Phys.* 17, 463 (1978).
- [31] A. Mishchenko, J. Berashevich, K. Wolf, D. A. Tenne, A. Reznik, and M. Mitkova, *Opt. Mater. Express*, OME 5, 295 (2015).
- [32] M. Mitkova, K. Wolf, G. Belev, M. Ailavajhala, D. A. Tenne, H. Barnaby, and M. Kozicki, *Phys Status Solidi (B) Basic Res* 253, 1060 (2016).
- [33] M. S. Ailavajhala, Y. Gonzalez-Velo, C. Poweleit, H. Barnaby, M. N. Kozicki, K. Holbert, D. P. Butt, and M. Mitkova, *Journal of Applied Physics* 115, 043502 (2014).
- [34] J. L. Taggart, Y. Gonzalez-Velo, D. Mahalanabis, A. Mahmud, H. J. Barnaby, M. N. Kozicki, K. E. Holbert, M. Mitkova, K. Wolf, E. Deionno, and A. L. White, *IEEE Transactions on Nuclear Science* 61, 2985 (2014).
- [35] T. Nichol, M. R. Latif, M. S. Ailavajhala, D. A. Tenne, Y. Gonzalez-Velo, H. Barnaby, M. N. Kozicki, and M. Mitkova, *IEEE Transactions on Nuclear Science* 61, 2855 (2014).
- [36] N. Habib, C. H. Lam, and R. McMahon, US8114686B2 (14 February 2012).
- [37] D. Lencer, M. Salinga, B. Grabowski, T. Hickel, J. Neugebauer, and M. Wuttig, *Nature Materials* 7, 972 (2008).
- [38] S. Bhosle, K. Gunasekera, P. Boolchand, and M. Micoulaut, *International Journal of Applied Glass Science* 3, 189 (2012).
- [39] S. Bhosle, K. Gunasekera, P. Chen, P. Boolchand, M. Micoulaut, and C. Massobrio, *Solid State Commun.* 151, 1851 (2011).
- [40] S. Ravindren, K. Gunasekera, Z. Tucker, A. Diebold, P. Boolchand, and M. Micoulaut, *J. Chem. Phys.* 140, 134501 (2014).
- [41] Lodovico, *PhysicsOpenLab* (2018).
- [42] J. Ziegler, *SRIM & TRIM* (n.d.).
- [43] J. Ziegler, J. Biersack, and M. Ziegler, *SRIM - The Stopping and Range of Ions in Matter*, 5th ed. (SRIM Co., n.d.).
- [44] X. Feng, W. J. Bresser, and P. Boolchand, *Phys. Rev. Lett.* 78, 4422 (1997).

- [45] Y. Wang, K. Tanaka, T. Nakaoka, and K. Murase, J. Non-Cryst. Solids 299–302, 963 (2002).
- [46] K. Murase, in *Insulating and Semiconducting Glasses* (2000).
- [47] K. Jackson, Physica Status Solidi (b) 217, 293 (2000).
- [48] R. Holomb, V. Mitsa, S. Akyuz, and E. Akalin, PHILOS MAG 93, 2549 (2013).
- [49] D. K. Avasthi and G. K. Mehta, in *Swift Heavy Ions for Materials Engineering and Nanostructuring*, edited by D. K. Avasthi and G. K. Mehta (Springer Netherlands, Dordrecht, 2011), pp. 47–66.
- [50] G. Yang, Y. Gueguen, J.-C. Sangleboeuf, T. Rouxel, C. Boussard-Plédel, J. Troles, P. Lucas, and B. Bureau, Journal of Non-Crystalline Solids 377, 54 (2013).
- [51] Crystallmaker, Crystallmaker.Com (n.d.).
- [52] P. Boolchand, G. Lucovsky, J. C. Phillips, and M. F. Thorpe, Philosophical Magazine 85, 3823 (2005).
- [53] M.-L. Theye, A. Gheorghiu, C. Senemaud, M. F. Kotkata, and K. M. Kandil, Philosophical Magazine B 69, 209 (1994).
- [54] P. K. Dwivedi, S. K. Tripathi, A. Pradhan, V. N. Kulkarni, and S. C. Agarwal, Journal of Non-Crystalline Solids 266–269, 924 (2000).
- [55] H. Takeuchi, O. Matsuda, and K. Murase, Journal of Non-Crystalline Solids 238, 91 (1998).
- [56] J. Rumble, *Handbook of Chemistry and Physics 101st Edition* (CRC Press, n.d.).
- [57] M. A. Abdel-Rahim, M. M. Hafiz, and A. M. Shamekh, Physica B: Condensed Matter 369, 143 (2005).
- [58] L. Filipovic, Topography Simulation of Novel Processing Techniques (n.d.).
- [59] E.-C. Inc, Properties of Silicon and Silicon Wafers Properties of Silicon and Silicon Wafers (n.d.).
- [60] Y. Wang, K. Tanaka, T. Nakaoka, and K. Murase, Physica B: Condensed Matter 316–317, 568 (2002).
- [61] A. Sharma, M. Varshney, H.-J. Shin, Y. Kumar, S. Gautam, and K. H. Chae, Chemical Physics Letters 592, 85 (2014).
- [62] N. C. Mishra, Radiation Effects and Defects in Solids 166, 657 (2011).
- [63] D. Simeone, D. Gosset, J. L. Bechade, and A. Chevarier, Journal of Nuclear Materials 300, 27 (2002).
- [64] B. Schuster, C. Trautmann, and F. Fujara, *Stabilization of High-Pressure Phase in HfO₂** (2011).
- [65] T. G. Edwards and S. Sen, J Phys Chem B 115, 4307 (2011).

Table 1:

Crystal thickness from XRD

Composition	Ion Energy (keV)	Crystals	Peak (2θ)°	Crystal Grain Thickness (nm)
Ge ₃₀ Se ₇₀	200	Orthorhombic GeSe	32.32	41.34
Ge ₃₀ Se ₇₀	200	Monoclinic GeSe ₂	29.6	35.44

Ge ₃₀ Se ₇₀	200	Hexagonal Se	42.98	38.82
Ge ₃₀ Se ₇₀	600	Monoclinic GeSe ₂	29.7	29.34
Ge ₃₀ Se ₇₀	600	Hexagonal Se	43.08	23.72
Ge ₃₀ Se ₇₀	1000	Monoclinic GeSe ₂	29.66	58.68
Ge ₃₀ Se ₇₀	1000	Hexagonal Se	43.1	44.94
Ge ₃₃ Se ₆₇	200	Orthorhombic GeSe	32.34	119.32
Ge ₃₃ Se ₆₇	200	Monoclinic GeSe ₂	29.66	47.78
Ge ₃₃ Se ₆₇	200	Hexagonal Se	43.08	21.86
Ge ₃₃ Se ₆₇	600	Monoclinic GeSe ₂	29.62	59.25
Ge ₃₃ Se ₆₇	600	Hexagonal Se	43.1	94.87
Ge ₃₃ Se ₆₇	1000	Orthorhombic GeSe	32.26	60.77
Ge ₃₃ Se ₆₇	1000	Monoclinic GeSe ₂	29.6	71.42
Ge ₃₃ Se ₆₇	1000	Hexagonal Se	43.04	47.42
Ge ₄₀ Se ₆₀	200	Orthorhombic GeSe	32.32	145.35
Ge ₄₀ Se ₆₀	200	Monoclinic GeSe ₂	29.64	43.69
Ge ₄₀ Se ₆₀	200	Hexagonal Se	43.12	40.66
Ge ₄₀ Se ₆₀	600	Orthorhombic GeSe	32.3	250.53
Ge ₄₀ Se ₆₀	600	Monoclinic GeSe ₂	29.66	43.24
Ge ₄₀ Se ₆₀	600	Hexagonal Se	43.04	37.11
Ge ₄₀ Se ₆₀	1000	Orthorhombic GeSe	32.3	51.67
Ge ₄₀ Se ₆₀	1000	Monoclinic GeSe ₂	29.6	37.33
Ge ₄₀ Se ₆₀	1000	Hexagonal Se	43.14	121.99

Table 2:

Calculation of DPA

Energy (keV)	Ge at.% (x)	Damage Rate (#/(cm.ion))	Time (sec)	Fluence (#/cm ²)	Charge, Q (C)	Area, A (cm ²)	Current, I(A)	Density (Atoms/cm ³)	DPA
200	30	3.40 x10 ⁸	900	4.92 x10 ¹⁴	1.6 x10 ⁻¹⁹	4	0.35μA	3.36 x10 ²²	4.98
200	33	3.35 x10 ⁸	900	4.92 x10 ¹⁴	1.6 x10 ⁻¹⁹	4	0.35μA	3.34 x10 ²²	4.94

200	40	3.60×10^8	900	4.92×10^{14}	1.6×10^{-19}	4	0.35 μ A	3.45×10^{22}	5.14
600	30	3.25×10^8	3108	4.88×10^{14}	3.2×10^{-19}	4	0.201 μ A	3.36×10^{22}	4.72
600	33	3.30×10^8	3108	4.88×10^{14}	3.2×10^{-19}	4	0.201 μ A	3.34×10^{22}	4.82
600	40	3.40×10^8	3108	4.88×10^{14}	3.2×10^{-19}	4	0.201 μ A	3.45×10^{22}	4.81
1000	30	3.00×10^8	11160	5.81×10^{14}	4.8×10^{-19}	4	0.1 μ A	3.36×10^{22}	5.19
1000	33	3.05×10^8	11160	5.81×10^{14}	4.8×10^{-19}	4	0.1 μ A	3.34×10^{22}	5.31
1000	40	3.25×10^8	11160	5.81×10^{14}	4.8×10^{-19}	4	0.1 μ A	3.45×10^{22}	5.48

List of Figures

Figure 1: Device Structure and operation

Figure 2: Raman spectra of $\text{Ge}_{30}\text{Se}_{70}$ under different irradiation. a) Amorphous b) Crystalline.

Figure 3: Raman spectra of $\text{Ge}_{33}\text{Se}_{67}$ under different irradiation. a) Amorphous b) Crystalline.

Figure 4: Raman spectra of $\text{Ge}_{40}\text{Se}_{60}$ under different irradiation. a) Amorphous b) Crystalline.

Figure 5: XRD of irradiated crystallized thin films. a) $\text{Ge}_{30}\text{Se}_{70}$ b) $\text{Ge}_{33}\text{Se}_{67}$ c) $\text{Ge}_{40}\text{Se}_{60}$

Figure 6: Ion penetration depth in chalcogenide glass (a-c) actual from simulation, (d) range.

Figure 7: Composition vs density and volume [50].

Figure 8: Peak damage rate vs composition.

Figure 9: Vacancy produced in Germanium and Selenium atoms.

Figure 10: $\text{Ge}_{40}\text{Se}_{60}$ Device Characterization. a) As-prepared b) 200keV c) 600keV d) 1000keV